International Journal of Applied Earth Observation and Geoinformation 124 (2023) 103541

Contents lists available at ScienceDirect

International Journal of Applied Earth Observation and Geoinformation

journal homepage: www.elsevier.com/locate/jag

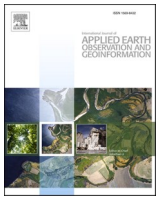

Advancing SAR monitoring of urban impervious surface with a new polarimetric scattering mixture analysis approach

Jing Ling [a,b], Shan Wei [a,b], Paolo Gamba [c,d], Rui Liu [a,b], Hongsheng Zhang [a,b,*]

[a] Department of Geography, The University of Hong Kong, Pokfulam, Hong Kong, China
[b] HKU Shenzhen Institute of Research and Innovation, Nanshan District, Shenzhen 518057, China
[c] Department of Electrical, Biomedical and Computer Engineering, University of Pavia, Pavia, Italy
[d] Pavia Research Unit, CNIT, Pavia, Italy

ARTICLE INFO

Keywords:
Urban impervious surface
Synthetic aperture radar
Scattering mixture

ABSTRACT

Accurate monitoring of urban impervious surfaces (UIS) changes is crucial in understanding the anthropogenic activities of urbanization and its environmental, economic, and social sustainability. Over the past two decades, synthetic aperture radar (SAR) has posed huge potential for urban monitoring with its all-weather and all-day imaging capability over rainy and cloudy regions around the world. Unfortunately, some critical challenges associated with UIS identification from data have been identified due to the high diversity of UIS and the different SAR imaging mechanisms from optical remote sensing. To address the challenges, this study proposed a new method of polarimetric scattering mixture analysis (PSMA) by modeling the diverse scattering mechanisms of various UIS categories. C- and L-band full-polarization SAR data in four typical urban areas from central, eastern, and southern China, were employed to evaluate the performance of the method. Experimental results demonstrate that the proposed method achieves an overall accuracy (OA) exceeding 96 % across all study cases. Compared with traditional methods, PSMA significantly reduces land cover confusion and enhances the producer's (PA) and user's accuracy (UA) for UIS, particularly for "road", by up to 13.4 % and 9.5 %, respectively. Non-impervious surfaces such as "soil" and "vegetation" witness a notable increase in PA and UA by up to 10 % and 20.5 %, respectively. These promising results underscore the effectiveness of the proposed method for accurate urban monitoring and understanding land cover scattering confusion over complex urban environments.

1. Introduction

Over the past years, global urbanization has rapidly increased, fueled by population growth and economic development. This phenomenon has been accompanied by significant changes in land cover and has had a profound impact on the global climate, ecosystems, and the environment (Mugiraneza et al., 2022). One critical indicator of anthropogenic interference is the prevalence of urban impervious surfaces (UIS) (Arnold and Gibbons, 1996). As urbanization is characterized by land cover changes from non-impervious surfaces (natural land covers) to impervious surfaces, monitoring the dynamic of UIS is crucial for understanding urban expansion and its social, economic, and environmental impacts and for promoting sustainable development (Shuster et al., 2005).

Satellite remote sensing provides an efficient means of observing land surfaces. Optical remote sensing has been a popular choice for a long time, as it offers numerous satellite data sources with varying spatial and spectral resolutions. However, optical remote sensing is highly susceptible to cloud contamination. Studies have shown that clouds cover approximately 67 % of the Earth's surface (King et al., 2013). Cities located in tropical and subtropical regions, where clouds persist throughout the year, are particularly affected by cloud contamination. In southern China, for example, only about 7.6 % of multispectral images are free from clouds within a year (Ling et al., 2021). Synthetic Aperture Radar (SAR) technology, which is capable of penetrating clouds, has attracted increasing attention as a solution to this problem (Dey et al., 2020; Lin et al., 2021; Samat et al., 2015). Full-polarization SAR (PolSAR), which transmits and receives fully polarized waves, is sensitive to objects' electrical conductivity and geometric structure and can provide discriminative information about the ground

* Corresponding author.
E-mail addresses: jingling@connect.hku.hk (J. Ling), shanw@connect.hku.hk (S. Wei), paolo.gamba@unipv.it (P. Gamba), rhysliu@connect.hku.hk (R. Liu), zhanghs@hku.hk (H. Zhang).

https://doi.org/10.1016/j.jag.2023.103541
Received 23 August 2023; Received in revised form 16 October 2023; Accepted 26 October 2023
Available online 3 November 2023

surface (Homayouni et al., 2019; Samat et al., 2018). Previous studies have reported the effectiveness of PolSAR for UIS extraction, focusing on various polarimetric decomposition methods, polarization mode, and classification techniques (Attarchi, 2020; Guo et al., 2014). There are also various methods for integrating optical and SAR data in land cover classification, typically falling into three primary levels: pixel level (Cao et al., 2019), feature level (Guo et al., 2014), and decision level fusion (Clinton et al., 2015), often involving machine learning and deep learning based classifiers (Ling and Zhang, 2023). However, cloud cover remains a persistent issue when optical data is involved.

Although existing SAR systems offer continuous and timely land surface observations, land cover confusion remains a significant issue in mapping using SAR data. In optical images, confusion between different land covers arises from spectral confusion, which has been widely explored and solved through various methods (Ridd, 1995; Tompkins et al., 1997; Wu and Murray, 2003). However, in PolSAR images, the mechanism of urban land cover confusion is entirely different. Scattering responses of urban land covers depend not only on the surface materials and their dielectric properties, but also on their shape, superficial roughness, position and orientation properties. This makes the traditional definition of land cover categories may not meet the actual situation of scattering behaviours in SAR images. Despite these differences, most PolSAR classification schemes still follow those proposed for optical data, with limited analysis on SAR scattering confusion and distinct SAR land cover categories exhibiting different scattering characteristics (Attarchi, 2020; Guo et al., 2014; Liu et al., 2019; Tan et al., 2020). Zhang et al. proposed an empirically developed land cover classification scheme for SAR data that achieved good performance (Zhang et al., 2018). However, a comprehensive understanding and quantitative analysis of land cover scattering for UIS identification in PolSAR still requires further exploration. This study aims to develop a new impervious surface classification method by conducting a comprehensive scattering mixture analysis and developing an urban land cover polarimetric scattering model accordingly. The main contributions of this study are:

(1) It provides a comprehensively qualitative and quantitative analysis of the polarization mechanisms and the polarimetric scattering mixture of complex urban land covers;
(2) it proposes an urban land cover polarimetric scattering model and a new impervious surface identification method based on scattering mixture analysis; and
(3) it provides a quantitative validation of the new model by applying it to different urban environments and to both C-band and L-band PolSAR imagery.

2. Study area and dataset

Over the past few decades, China has experienced rapid urbanization, leading to significant changes in land cover, particularly with respect to impervious surfaces that reflect the country's development and prosperity. However, optical observation of impervious surfaces in many areas of China poses significant challenges due to year-round cloud cover. Therefore, it is essential to explore effective methods to improve impervious surface identification using SAR systems. This study focuses on four cities with different urban environments. Hong Kong (HK) is one of the busiest and most efficient international coastal cities with a high degree of urbanization. Shenzhen (SZ) is one of the largest

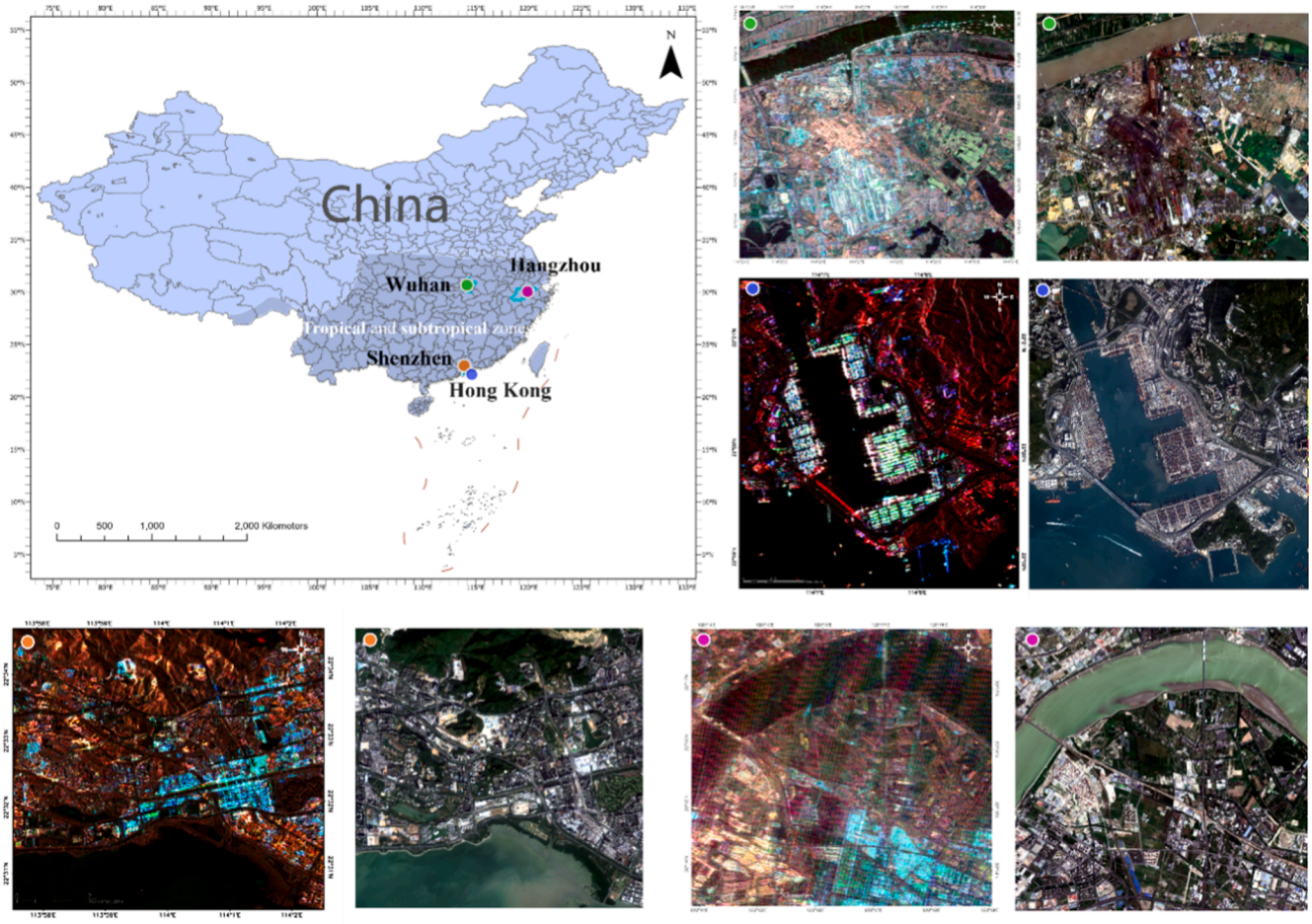

Fig. 1. Location and ALOS-2 images of Shenzhen, Hangzhou, Hong Kong, and Wuhan.

cities in Mainland China, which has undergone rapid land cover changes. Hangzhou (HZ) is located south of the Yangtze River Delta in Eastern China. This city is low-lying and densely covered with crops and river networks. Wuhan (WH), located in central China, is the geographical center of the Chinese economy. Here various land covers are interlaced with dense urban architecture. Fig. 1 presents the SAR images of the four test sites, displayed as false-color images, where the RGB values correspond to the HV, VV, and HH backscattering coefficient intensities. The land cover types in SZ, HZ, and WH mainly comprise vegetation, buildings, roads, soil, and water. However, in HK, in addition to these more typical classes, the "port" is a unique and distinctive land cover type.

The study utilized L-band fully polarimetric ALOS-2 images with a 5-m resolution and C-band fully polarimetric GF-3 images with an 8-m resolution. The ALOS-2 and GF-3 images for SZ and HK were obtained in November 2017 and December 2018, respectively. In HZ and WH, single ALOS-2 images were used due to data availability limitations, with the acquisition time in August 2020 and August 2019, respectively. The ALOS-2 image dimensions are 3097 × 2736 for Wuhan, 1872 × 1652 for Hangzhou, 1671 × 1525 for Shenzhen, and 934 × 1044 for Hong Kong. Additionally, GF-3 images have dimensions of 1042 × 883 for Shenzhen and 584 × 653 for Hong Kong.

The fully polarimetric SAR images underwent preprocessing with the SNAP software, followed by the application of the enhanced Lee filter to reduce speckle noise. Finally, the processed ALOS-2 and GF-3 images, along with their extracted polarimetric features, were geocoded under the WGS84 and UTM georeferenced system. The two images were co-registered with over 20 manually selected ground control points, with a registration error of less than 1 pixel. Additionally, high-resolution optical images from Worldview-2 (1.6 m spatial resolution) obtained in April 2018 (for SZ and HK), Sentinel-2 images (10 m spatial resolution) obtained in August 2020 (for HZ) and August 2019 (for WH), and Google Earth images acquired close to the PolSAR images were used for reference.

3. Methodology

3.1. Polarimetric scattering mixture analysis (PSMA)

Urban land surfaces, generally split into four types - soil, water, vegetation, and UIS, are defined by their urban functional properties and surface material properties in optical remote sensing. However, in SAR images, the situation is completely distinct, as elucidated earlier. Due to the dependency on shape, superficial roughness, position and orientation properties, the same urban land cover surface, composed of the same surface material, can produce widely different scattering responses. Therefore, elemental scattering compositions, shape, roughness, position, and orientation should be adopted to describe the land surface scattering response.

To this aim, it is usual to refer to the polarimetric scattering matrix, which characterizes the complex electromagnetic interaction process and provides abundant information:

$$[S] = \begin{bmatrix} S_{HH} & S_{HV} \\ S_{VH} & S_{VV} \end{bmatrix} \tag{1}$$

where S_{XY} denotes the X-polarization mode of transmission and the Y-polarization mode of reception. Based on the symmetric assumption between the HV and VH cross-polarized modes, the coherence matrix $\boldsymbol{T}$, which contains full polarization information, can be derived from the scattering matrix and expressed as

$$T = \begin{bmatrix} T_{11} & T_{12} & T_{13} \\ T_{21} & T_{22} & T_{23} \\ T_{31} & T_{32} & T_{33} \end{bmatrix} = \frac{1}{2}\begin{bmatrix} \langle |S_{HH}+S_{VV}|^2 \rangle & \langle (S_{HH}+S_{VV})(S_{HH}-S_{VV})^* \rangle & 2\langle (S_{HH}+S_{VV})S_{HV}^* \rangle \\ \langle (S_{HH}-S_{VV})(S_{HH}+S_{VV})^* \rangle & \langle |S_{HH}-S_{VV}|^2 \rangle & 2\langle (S_{HH}-S_{VV})S_{HV}^* \rangle \\ 2\langle S_{HV}(S_{HH}+S_{VV})^* \rangle & 2\langle S_{HV}(S_{HH}-S_{VV})^* \rangle & 4\langle |S_{HV}|^2 \rangle \end{bmatrix} \tag{2}$$

where $\boldsymbol{T}_{ij}$ is the element of $\boldsymbol{T}$ in row i and column j. Diagonal elements $\boldsymbol{T}_{11}$, $\boldsymbol{T}_{22}$, and $\boldsymbol{T}_{33}$ refer to three fundamental scattering mechanisms: surface scattering, double-bounce scattering, and volume scattering, respectively. The decomposition of PolSAR can help reveal the scatter's backscattering information in more detail and thus better study the components with different scattering mechanisms of various urban land covers. Freeman-Durden decomposition (Freeman and Durden, 1998), Cloude-Pottier decomposition (Cloude and Pottier, 1996), and Yamaguchi four-component decomposition (Yamaguchi et al., 2005) mainly explain the target scattering mechanisms in surface scattering, double-bounce scattering, and volume scattering. H/A/α decomposition (Pottier and Cloude, 1997) derives H, A, and α as follows to quantitatively depict the scattering response:

$$H = -\sum_{i=1}^{3} P_i \log_3 P_i \tag{3}$$

$$A = \frac{\lambda_2 - \lambda_3}{\lambda_2 + \lambda_3} \tag{4}$$

$$\alpha = P_1\alpha_1 + P_2\alpha_2 + P_3\alpha_3 \tag{5}$$

$$P_i = \frac{\lambda_i}{\sum_{i=1}^{3}\lambda_i} \tag{6}$$

where the parameter α_i is associated with the surface angle of incidence and dielectric constant, parameter λ_i is the calculated eigenvalue of the coherence matrix $\boldsymbol{T}$, and P_i is the appearance probability of each λ_i. The entropy H measures the randomness of the scattering process, and the scattering angle α measures the type of scattering mechanism.

Based on the physical principles of polarimetric SAR scattering, the aim is to develop a model for polarimetric scattering mixture analysis that can represent the scattering response of ground surfaces using three fundamental scattering mechanisms (surface scattering, double-bounce scattering, and volume scattering) and their respective scattering effectiveness:

$$S = \sum_{i=1}^{3} \omega_i BM_i E_i \tag{7}$$

where S is the surface scattering response, BM_i is the i-*th* basic scattering mechanism, ω_i is the intensity of BM_i, and E_i is the probability of the effectiveness of BM_i. This formula serves as a conceptual representation to bridge the theoretical understanding from prior research (Pottier and Cloude, 1997) with the practical polarimetric scattering mixture analysis in this study, facilitating the following construction of the urban land cover scattering model and identification of scattering subcategories with unique scattering characteristics.

3.2. Urban land cover scattering modeling

Building upon theoretical foundations that interpret land surface scattering responses using three fundamental polarimetric scattering mechanisms and their respective scattering randomness, as well as the understanding of complex land cover scattering based on polarimetric

scattering mixture analysis, this study proposes an urban land cover polarimetric scattering conceptual model. Fig. 2 illustrates the proposed urban land cover polarimetric scattering model, which shows the distribution of the identified UIS and other land cover scattering subcategories on the H- α scattering space. The H- α plane is independent of the probability density distribution and covers all scattering mechanisms. As the value of the scattering angle α (vertical axis) increases continuously from 0 to 90°, the corresponding scattering mechanism switches from surface scattering to volume scattering and then to double-bounce scattering. H represents the entropy and measures the scattering randomness, with greater randomness indicating weaker scattering efficacy. The increase of entropy H (horizontal axis) from 0 to 1 describes the rise of scattering randomness. Based on the physical characteristics of H and α, as developed in previous research (Pottier and Cloude, 1997; Zhang et al., 2018), the entire scattering plane can be divided into nine zones according to their split criteria. Each zone of Z1-Z8 in Fig. 2 describes a scattering basis (Z9 is nonfeasible).

Table 1 provides detailed descriptions of the corresponding land cover scattering sub-categories. These sub-categories include building (BU1, BU2, BU3, BU4), port (PO1, PO2, PO3), roads (RO1, RO2, RO3, RO4), soil (SO1, SO2, SO3), vegetation (VE1, VE2, VE3), and water (WA1, WA2, WA3). Among the four building subtypes, BU1 is located in zones 1 and 4 on the H-α plane, and refers to double-bounce scattering buildings with low to medium scattering randomness, mainly sparse buildings aligned in the radar system's viewing direction and forming a dihedral angle between the wall and the ground. BU2 denotes anisotropic buildings, mainly dense buildings that are not parallel to the radar flight direction. BU2 falls within zones 2 and 5, indicating a volume scattering mechanism, but with low to medium scattering randomness. BU3 is located in zones 3 and 6, and it includes buildings with smooth roofs. Finally, BU4 includes buildings with complex structures, such as dense and small buildings with irregular alignment, which exhibit high randomness scattering and are located in zones 7 and 8.

Regarding roads, RO1 mainly includes vertical facilities located on the road, such as viaducts, overpasses, highway guardrails, and even the dihedral angle formed by the road and thick tree trunks along the road borders. RO1 falls within zones 1 and 4 and is characterized by double bounce scattering with low to medium scattering randomness. RO2 (located in zones 2/5) mostly includes rough asphalt or concrete road surfaces and pavement mixtures, causing volume scattering with low to medium scattering randomness. RO3 mainly includes roads with smooth surfaces, causing surface scattering. Finally, RO4 falls within zones 7 and 8 and is characterized by high entropy. It includes complex structural roads, such as various traffic facilities on the road and low vegetation in the middle of the road.

As for the port classes, PO1, PO2, and PO3 fall within zones 1 and 4, zones 2 and 5, and zones 3 and 6, respectively. PO1 represents containers forming double-bounce scattering with the ground, while PO2 includes dense containers with anisotropic reflectors. PO3 represents containers with a smooth top.

Vegetation is divided into three sub-categories: VE1 (zones 1/4/7), VE2 (zones 3/6), and VE3 (zones 5/8), representing trees with double reflectors such as stout tree trunks, vegetation with leaves forming flat surfaces, and random anisotropic vegetation such as the crown structure of lush foliage, respectively. Due to their different shapes, scattered heights, leafy branches, and leaves, vegetation exhibits a very complex scattering behavior. When vegetation forms a dihedral angle with the ground, it can be mistaken for UIS.

The soil class is divided into SO1 (zones 1/4/7), SO2 (zones 2/5/8), and SO3 (zones 3/6). SO1 refers to double reflections because of surrounding tree trunks or buildings. SO2 denotes soil with uneven surfaces, especially soil in construction areas. SO3 represents soil with flat surfaces.

Finally, water not only shows surface scattering (WA2) as generally known, but it can also show double bounce scattering when the water surface forms a dihedral angle with the ships and the shore, a case denoted as WA1 (zones 1/4). Waves can also cause water to exhibit volume scattering with medium entropy, located in zone 5 (WA3).

According to the land cover scattering model, we propose a classification framework that is divided into three levels, as described in detail in Table 1. Level I aims to distinguish between the two fundamental land surface categories: impervious and non-impervious surfaces. Traditional land cover classification schemes typically divide urban land covers into four types: vegetation, soil, water, and UIS. Considering the significant scattering and functional difference, the proposed fine-UIS oriented land cover classification scheme (level II) divides UIS into three fine-UIS types (buildings, port, and roads) to reduce the heterogeneity of the UIS label and thus mitigate confusion. Another advantage of this fine-UIS scheme is that these subclasses are associated with various urban functions, providing more social and economic information than

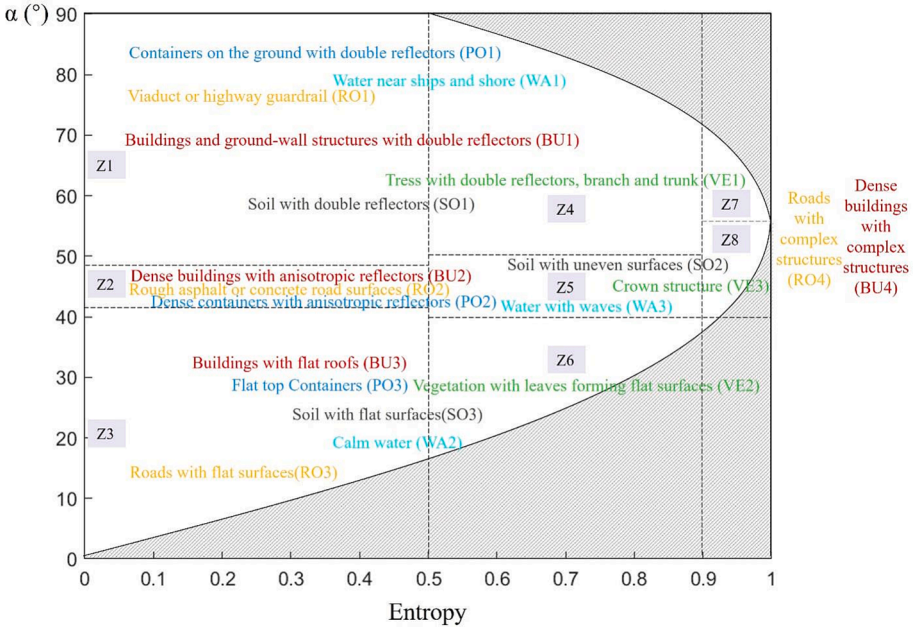

Fig. 2. The polarimetric scattering distribution of urban land covers.

Table 1
Descriptions of different land cover scattering categories.

Land cover types	Fine-UIS oriented Land cover types	Land cover scattering sub-types	Description
Urban impervious surfaces (UIS)	Building	BU1	Double bounce scattering buildings with low to medium scattering randomness, located in zone 1&4.
		BU2	Anisotropic buildings with volume scattering, located in zone 2&5.
		BU3	Surface scattering buildings with low to medium scattering randomness, located in zone 3&6.
		BU4	High randomness scattering buildings, located in zone 7&8.
	Road	RO1	Double bounce scattering roads with low to medium scattering randomness, located in zone 1&4.
		RO2	Volume scattering roads with low to medium scattering randomness, located in zone 2&5.
		RO3	Surface scattering roads, located in zone 3&6.
		RO4	High randomness scattering roads, located in zone 7&8.
	Port	PO1	Containers forming double bounce scattering with the ground, located in zone 1&4.
		PO2	Volume scattering port, located in zone 2&5.
		PO3	Surface scattering port, located in zone 3&6.
Non-impervious surfaces (NIS)	Vegetation	VE1	Double reflection propagation vegetation, located in zone 1&4&7.
		VE2	Surface scattering vegetation, located in zone 3&6.
		VE3	Random anisotropic vegetation, located in zone 5&8.
	Soil	SO1	Double reflector soil, located in zone 1&4&7.
		SO2	Volume scattering soil, located in zone 2&5&8.
		SO3	Surface scattering soil, located in zone 3&6.
	Water	WA1	Double bounce scattering water, located in zone 1&4.
		WA2	Surface scattering water, located in zone 3&6.
		WA3	Volume scattering with medium entropy, located in zone 5.

traditional land cover classification schemes. Finally, compared to the optical VIS model, the finest level (level III) identifies land cover scattering sub-categories based on polarimetric scattering mixture analysis.

3.3. Impervious surface mapping based on PSMA

The impervious surface mapping framework of this study is shown in Fig. 3, demonstrating the proposed impervious surface identification flowchart. For feature extraction, the Freeman-Durden decomposition (Freeman and Durden, 1998), the Cloude-Pottier decomposition (Cloude and Pottier, 1996), the Yamaguchi four-component decomposition (Yamaguchi et al., 2005), and the H/A/α decomposition (Pottier and Cloude, 1997) were considered. The different polarization decomposition parameters, the coherence matrix diagonal elements T_{11}, T_{22}, T_{33}, and the backscattering coefficients for HH, HV, VH, and VV were all considered as polarimetric features for classification. With the established urban land cover scattering model, land surface classification was first conducted at the level of the sub-classes. Then, adopting a merging strategy, land cover scattering sub-classes were combined into six fine-UIS oriented land covers, and finally merged into binary UIS and non-impervious surfaces (NIS) maps to extract impervious surface extents. The Transformer network has garnered considerable attention in both natural language processing and computer vision domains due to its superior performance (Devlin et al., 2018; Vaswani et al., 2017). In particular, the Swin Transformer (Liu et al., 2021), a recent visual Transformer backbone network combining the powerful modeling capabilities of the Transformer structure with essential visual signal priors, has achieved remarkable breakthroughs in tasks such as object detection and semantic segmentation. Motivated by these notable achievements, we leverage the Swin Transformer as the classifier in our proposed model to effectively utilize scattering properties for identifying distinct land cover scattering subcategories.

Experimental samples were labelled by visual interpretation of high-resolution Google Earth images, Worldview-2 optical images, and Sentinel-2 optical images near the acquisition date of the corresponding PolSAR images. Moroever, three field surveys were conducted, including two surveys in HK in March and June 2019 and one in SZ in November 2020. Photos of different land covers were collected. Then, we performed extensive manual labeling, aided by high-resolution satellite imagery, expert knowledge and field surveys. For ALOS-2 data in WH and HZ, [21761, 17455, 17981, 12974, 6884] and [12854, 9141, 11950, 7436, 9015] samples were labeled for building, road, vegetation, soil, and water classes, respectively. Instead, 35031, 22773, 18636, 7932, and 16,765 samples were labeled for building, road, vegetation, soil, and water and applied to ALOS-2 data in SZ. Note that the sample locations for GF-3 in SZ are the same as those for ALOS-2 data, but since the resolution of GF-3 is 8 m, its sample number is lower than the one for ALOS-2 (5 m resolution), which is 13365, 9389, 7149, 3185, and 6285. In HK, the samples applied to ALOS-2 data are 22642, 18245, 10026, 19421, 2388, and 20017, for building, port, road, vegetation, soil, and water, respectively, corresponding to 9059, 7199, 4310, 4182, 903, and 7773 samples for GF-3. We meticulously ensured that these samples were as evenly distributed as possible across the entire study area and that the samples within each class were relatively balanced, mitigating potential biases and other confounding factors. Finally, for each experiment, a random 80 % of the sample was used for classifier training, and the remaining 20 % was exploited for performance evaluation.

4. Results

In this section, three different experiments were conducted. Firstly, the urban land cover polarimetric scattering mixture and the proposed urban land cover scattering model were analyzed quantitatively. Secondly, the established sample set was used to evaluate the classification accuracy of the proposed scattering-mixture-analysis-based UIS classification system in HK, WH, HZ, and SZ using ALOS-2 and GF-3 images. A set of assessment metrics, including overall accuracy (OA), user's accuracy (UA), producer's accuracy (PA), and confusion matrix, were utilized for comprehensive evaluation. Finally, classification results were mapped over the entire study area with ALOS-2 and GF-3 at different levels of land cover types for a qualitative analysis. In both quantitative and qualitative evaluations, the results of the proposed classification system were compared with those of more traditional state-of-the-art procedures to validate its effectiveness, with the same classifier and experimental settings.

4.1. Urban land cover polarimetric scattering analysis

To explore the scattering response of the urban land covers, a color-coded scattering space is proposed in Fig. 4. In Fig. 4 (a), class samples

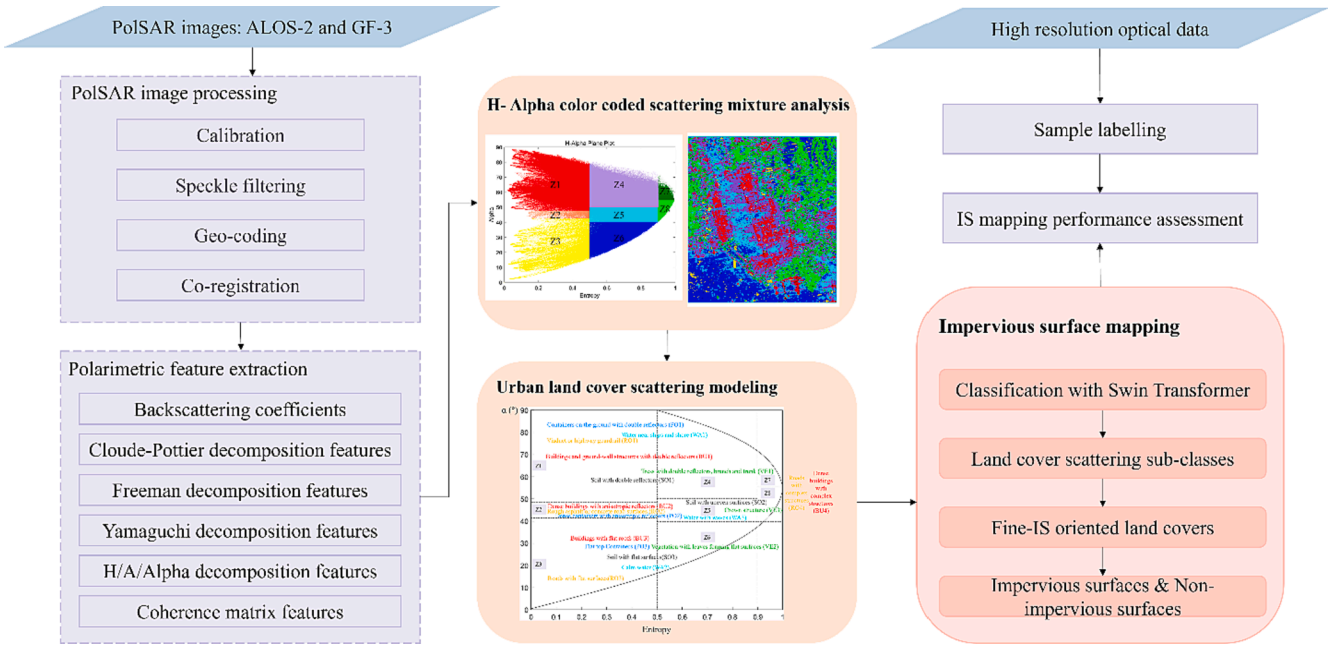

Fig. 3. Urban impervious surface mapping framework.

are identified by their value of entropy and alpha in the H-α Plane. A color-coded scattering space was created in which eight basic zones were represented with different colors, as seen in Fig. 4 (b). Colors indicate various types of basic scattering behavior, and each sample in the SAR image is colored accordingly. The color-filled ALOS-2 and GF-3 images of HK and SZ are presented in Fig. 4 (c-f).

Fig. 4 (c-f) clearly illustrates that the conventional understanding of land cover distribution on the H- α plane, such as water in Z3, does not accurately capture the complex reality. Instead, the water area shows four distinct colors, indicating four different scattering behaviors. The seawater located far away from the urban area is relatively calm and characterized by a reflected surface scattering with low entropy (yellow). Waters at a medium distance from the metropolitan area are affected by wind and show a reflected surface scattering with medium entropy (dark blue). Water samples near the urban area are more susceptible to waves caused by passing ships and wind, resulting in volumetric scattering (light blue). Finally, water areas very close to the port exhibit double bounce scattering (purple) due to the dihedral angle between the water surface and the port infrastructures. In summary, the scattering mixture of the land surfaces is complex. The same land cover shows multiple different scattering behaviors according to the urban environment, and most traditional knowledge of the land cover scattering behavior is not fully and easily applicable.

Fig. 4 also prominently displays the considerable diversity in SAR

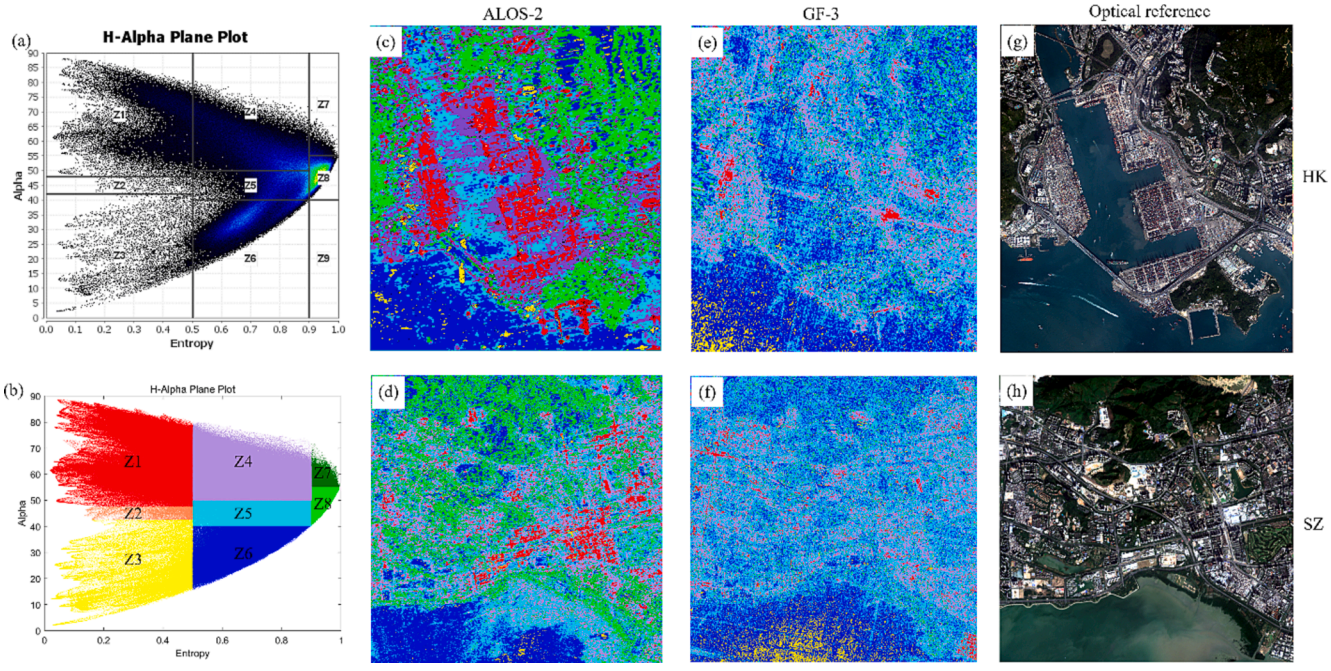

Fig. 4. Color-coded scattering mixture analysis of the study area. (a) H- α Plane. (b) Color-coded scattering space. (c-f) Color-filled SAR images. (g-h) Optical images of HK and SZ for reference.

data between the L-band ALOS-2 and C-band GF-3. This diversity can be attributed to the difference in wavelength between L-band SAR (wavelength ≈ 23 cm) and C-band SAR (wavelength ≈ 5.5 cm). L-band SAR can penetrate vegetation and soil to some extent, capturing information from beneath the surface, while C-band SAR is more sensitive to surface structures. Notably, most vegetation is mapped as light green in ALOS-2 while in light blue in GF-3. This difference can be explained by the distinct scattering characteristics of vegetation at L-band and C-band frequencies. In C-band, backscattering primarily occurs due to the interaction with the vegetation canopy, while in L-band, it is scattered with lower leaves and trunks, resulting in higher scattering randomness. As a result, the same type of vegetation can appear differently in the two datasets. Similarly, buildings tend to be mapped in red in ALOS-2 while in purple in GF-3. This variation may be attributed to the differences in how C-band and L-band SAR interact with built structures, as well as the impact of surrounding vegetated surfaces. The low penetration of C-band SAR is more easily disrupted by vegetated surfaces, such as trees near buildings, which can affect the observed scattering responses.

Fig. 5 shows the scattering plane density distribution of each fine-UIS-oriented land cover with both ALOS-2 and GF-3 images in HK and SZ. Obviously, each land cover had distribution on multiple H- α zones. 'Building' and 'road' even had distribution in all eight zones, while 'building' and 'port' were more likely to be distributed in the double bounce scattering areas. 'Soil' had multiple scattering behavior. 'Vegetation' was concentrated in volume scattering with medium and high entropy. And 'water' was more likely to be distributed in surface scattering with medium entropy.

Fig. 6 presents a land cover class probability distribution on the scattering plane, indicating the category of land cover with the highest probability of presenting the scattering behavior corresponding to the H-α location. Generally, surface scattering tended to be reflected by 'road' and 'water', although the low entropy zone was more likely to be occupied by 'road' rather than 'water', which might be due to the sea waves of 'water'. Double bounce scattering was observed to be reflected by 'port' and 'building' because of the dihedral angle between the wall and ground. Volume scattering with medium and high entropy was typically reflected by 'vegetation', as well as 'soil' and 'building.'.

4.2. Validation of detailed land cover scattering behavior

To investigate further the distinctive scattering characteristics of the land covers and their underlying causes, Fig. 7 (a) (b) demonstrates the color-coded scattering distribution of each land cover along with their corresponding color-filled real land positions, overlaid on the H-a-alpha feature base map. Columns (c-e) show zoomed-in details of the color-filled land positions, the H-a-alpha feature map, and the optical reference image.

Fig. 7 (a) illustrates that most land covers are spread across multiple zones, but there are specific differences seen from Fig. 7 (b-e). Regular and flat buildings tended to exhibit double bounce scattering, while patchy buildings or those surrounded by vegetation demonstrated medium to high entropy and volume scattering. A few smooth roofs displayed surface scattering with medium entropy. The 'Port' area often showed low to medium entropy double bounce scattering. However, low to medium entropy volume and surface scattering also occurred in staggering containers. The side of roads close to buildings typically exhibited low to medium entropy double bounce scattering, while the side close to vegetation showed medium entropy volume scattering or even high entropy scattering. Smooth roads in a few locations might also exhibit surface scattering. Vegetation usually exhibited medium to high entropy volume scattering and displayed double bounce scattering near buildings or thick trunks along roadsides. Additionally, vegetation showed surface scattering in some places due to smooth foliage. The soil exhibited medium entropy surface or volume scattering but also showed double bounce scattering near buildings or thick branches and high entropy scattering near low vegetation. Sea water far from urban areas demonstrated surface scattering, but waves could cause medium entropy volume scattering, while dihedral angles with the coast might cause double bounce scattering. In summary, the comparison of the scattering behaviors with the real land ground situation validates the diverse scattering patterns of urban land covers and their underlying factors. This substantiates the significance of the proposed PSMA method.

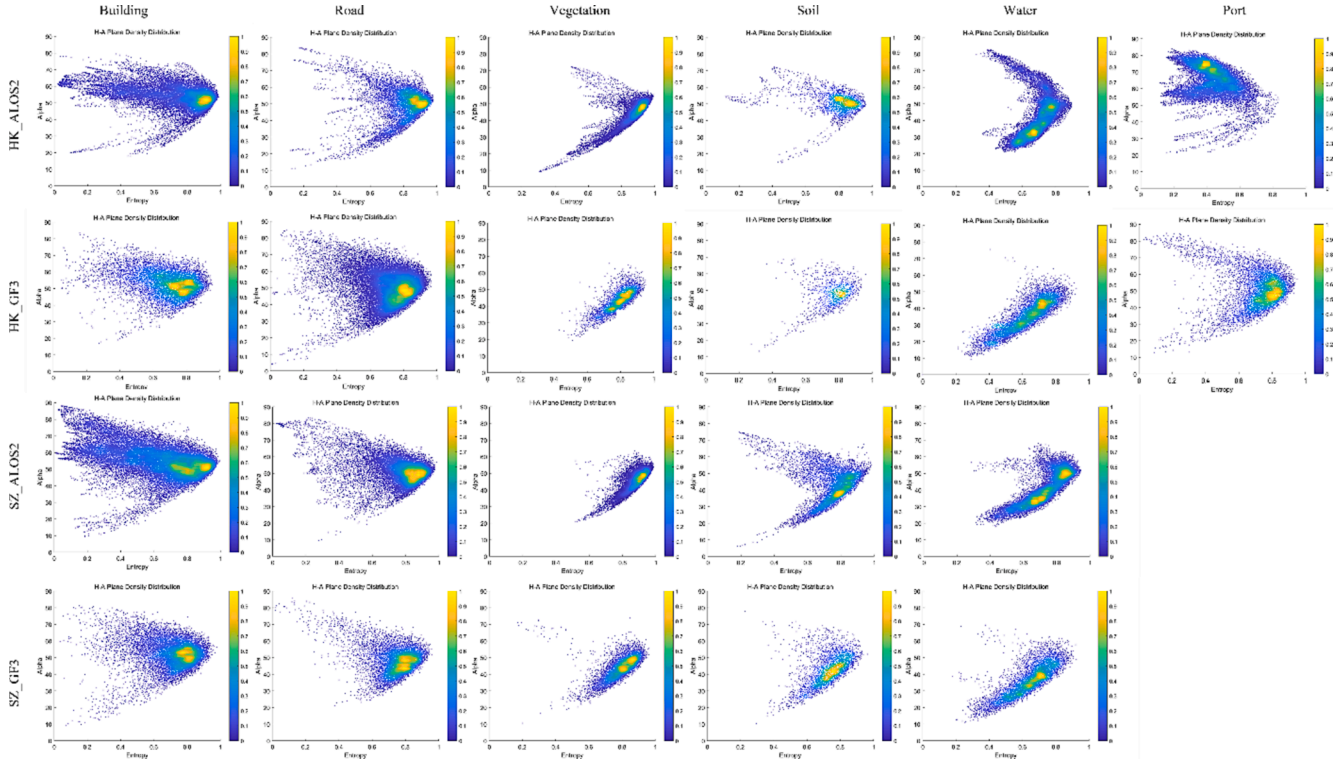

Fig. 5. H- α density distribution of each land cover in HK and SZ with ALOS-2 and GF-3.

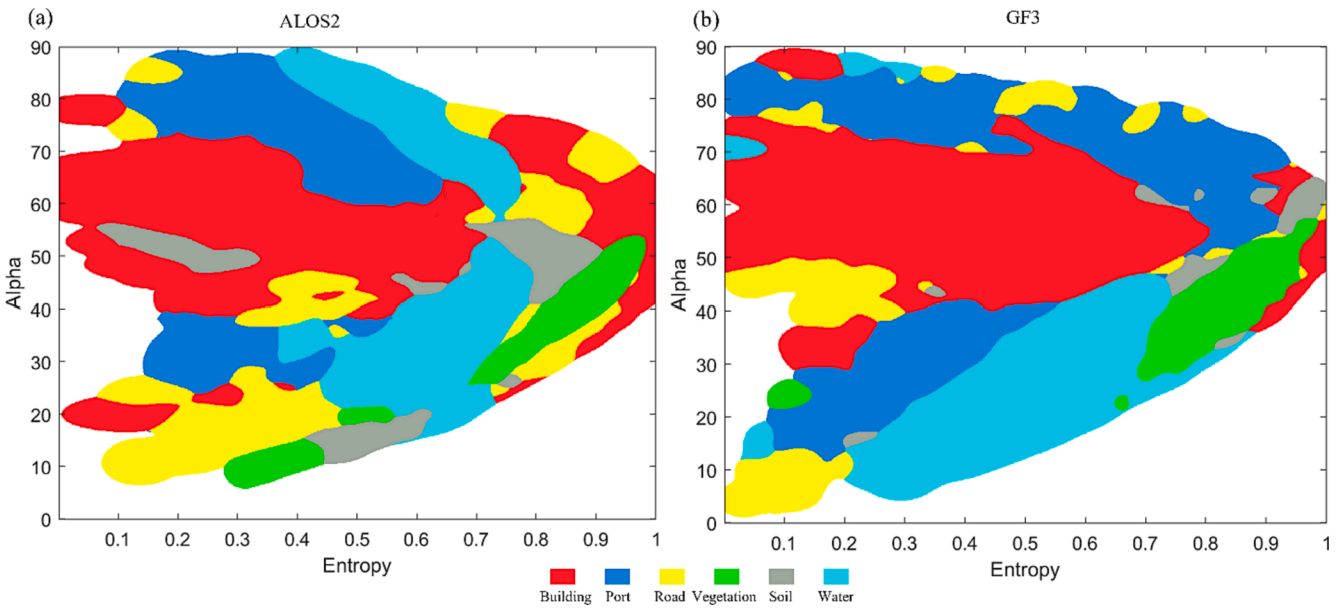

Fig. 6. Probability distribution of land cover classes on scattering plane with ALOS-2 (a) and GF-3 (b).

Fig. 8 shows the 17-dimensional mean polarimetric features of each land cover in different H- α zones. It indicates that not only do different H- α zones exhibit variations in H- α space, but these zones also display differences in other polarimetric features. This observation further demonstrates that multiple scattering behaviors are mixed within traditionally defined land covers.

To assess the rationality of the identified land cover scattering sub-categories, a quantitative investigation of the separability between the H- α zones for each land cover was conducted and presented in Fig. 9. The Jeffries–Matusita (JM) distance (Dabboor et al., 2014), a widely applied measure of separability, was used in this study to evaluate the separability between the H- α zones. The JM distance ranges between 0 and 2, with higher values indicating greater separability between H- α zones.

The quantitative investigation results in Fig. 9 confirmed that the identified H-α scattering sub-categories were rational and meaningful. Although slight differences were observed between different study areas and polarization SAR data, the overall distribution of separability was consistent. The separability between the Z1 and Z4 zones was relatively small for all land covers, indicating that the difference between the medium and low entropy scattering mechanisms might not be significant under the double bounce scattering mechanism. The same phenomenon could be found in Z3 and Z6. The double bounce (Z7) and volume (Z8) scattering with high entropy also showed low separability under the two fine-UIS categories' Building' and 'Road'. For soil and vegetation, the separability between Z4 and Z7 (and Z5 and Z8) was relatively low. These results were consistent with the proposed scattering sub-categories for each land cover.

In conclusion, the traditional land cover classification schemes, which divide land covers into four categories based on spectral properties, are not sufficient for SAR imagery. The above detailed analysis of scattering behavior of land covers has demonstrated the existence of purer land cover sub-categories that exhibit unique scattering properties. The proposed method, based on the identification of scattering sub-categories, has been validated by the consistency of its results with real land surface scattering responses.

4.3. Classification accuracy evaluation

In addition to the land cover classification based on the proposed land cover scattering sub-category system, other classification schemes were also implemented for comparative analysis. The fine-UIS oriented land cover system and 2-class UIS-NIS system were utilized for this purpose, and the classification was performed using the same classifier and samples.

The proposed scattering-based classification system was employed to classify the land surface. The confusion matrices of land cover scattering subclasses in Hong Kong (HK), Shenzhen (SZ), Wuhan (WH), and Hangzhou (HZ), obtained from ALOS-2 and GF-3 data, are presented in Fig. 10 (a-f). Several observations can be made from these matrices. The majority of confusion observed among sub-categories sharing the same scattering mechanism, such as BU1, PO1, RO1, VEG1, and SO1, as well as BU2, PO2, RO2, and VEG3, underscores a key point. This confusion primarily arises because urban land covers can manifest multiple scattering behaviors, and different land cover types may exhibit similar scattering characteristics. While it's acknowledged that scattering sub-categories of different land cover types may overlap within the same scattering zone, the identification of these sub-categories with specific scattering properties plays a vital role. This identification helps reduce intra-class variance within land cover categories and enhances our ability to discriminate between land cover types based on their unique scattering properties. Additionally, differences were observed in the distribution of land cover scattering sub-categories between ALOS-2 and GF-3 data. For instance, in ALOS-2, most port samples were classified as PO1, while in GF-3, these samples were more evenly distributed among PO1, PO2, and PO3. This finding aligns with the H-α density distribution depicted in Fig. 5 and can be attributed to variations in polarization frequency, polarization band (C and L), and angle of incidence between the two radar systems.

The land cover scattering sub-categories were then aggregated into fine-UIS-oriented land cover categories for further analysis, as depicted in Fig. 10 (g-l). Misclassifications of buildings and roads as vegetation constituted a substantial portion of the confusion between UIS and NIS, likely attributable to trees planted alongside roads and buildings in complex urban environments. Soil often exhibited confusion with bright impervious surfaces in optical images because of its high spectral reflectance. Although the confusion mechanisms between spectral and scattering characteristics differ, the challenge of distinguishing soil from UIS (especially roads) persists in PolSAR images due to the complexity of soil scattering, as illustrated in Fig. 7. Dry and flat soil may be misclassified as roads, while uneven soil surfaces, soil undergoing construction or overlaid with manufactured objects, and shallow grass could

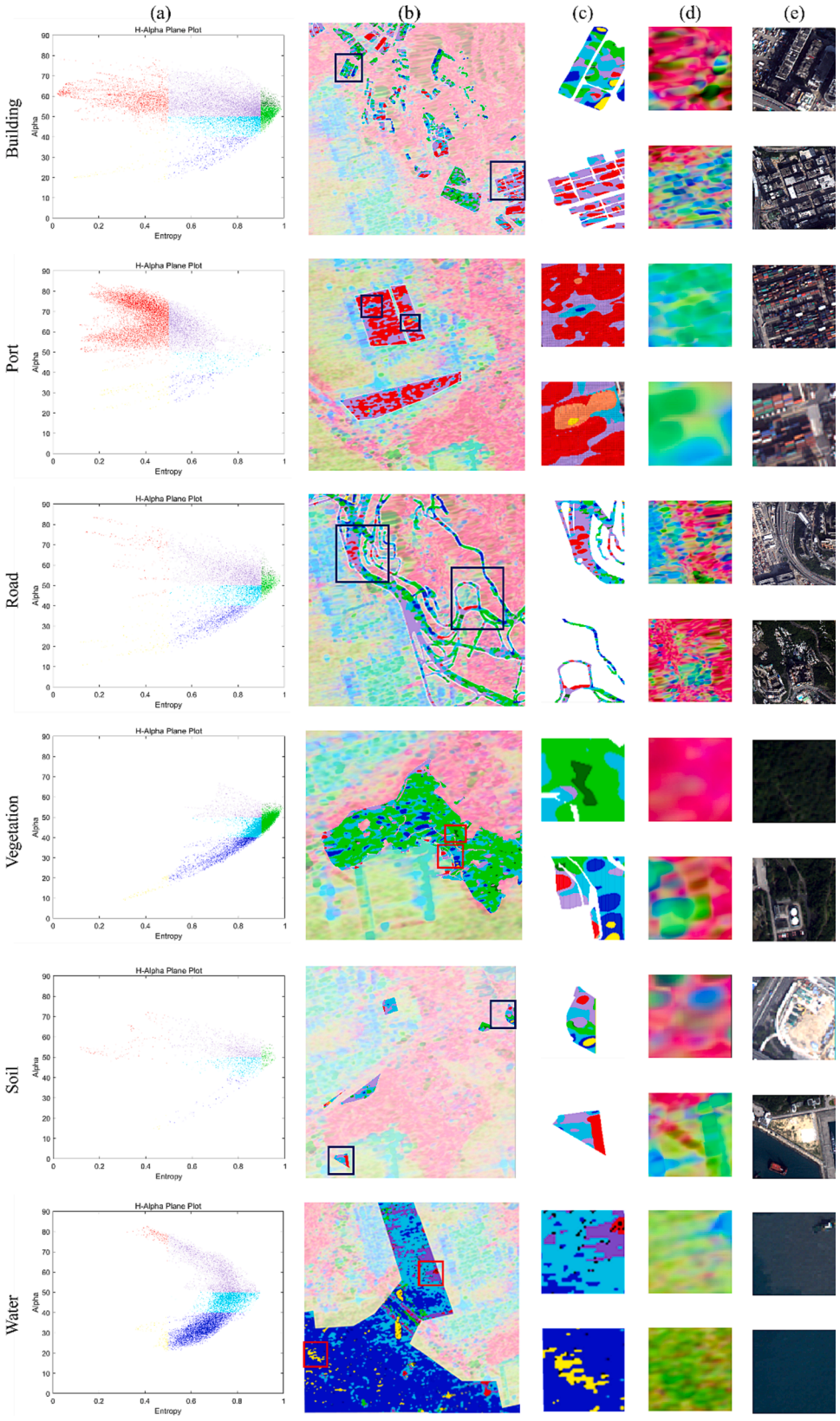

Fig. 7. Color-coded scattering distribution and the corresponding color-filled land positions of each land cover. Column (a) shows the color-coded scattering distribution of each land cover, and column (b) displays the color-filled positions of the land cover superimposed the H-a-alpha feature base map. Columns (c-e) present the detailed color-filled positions, the H-a-alpha feature map, and the optical reference image, respectively.

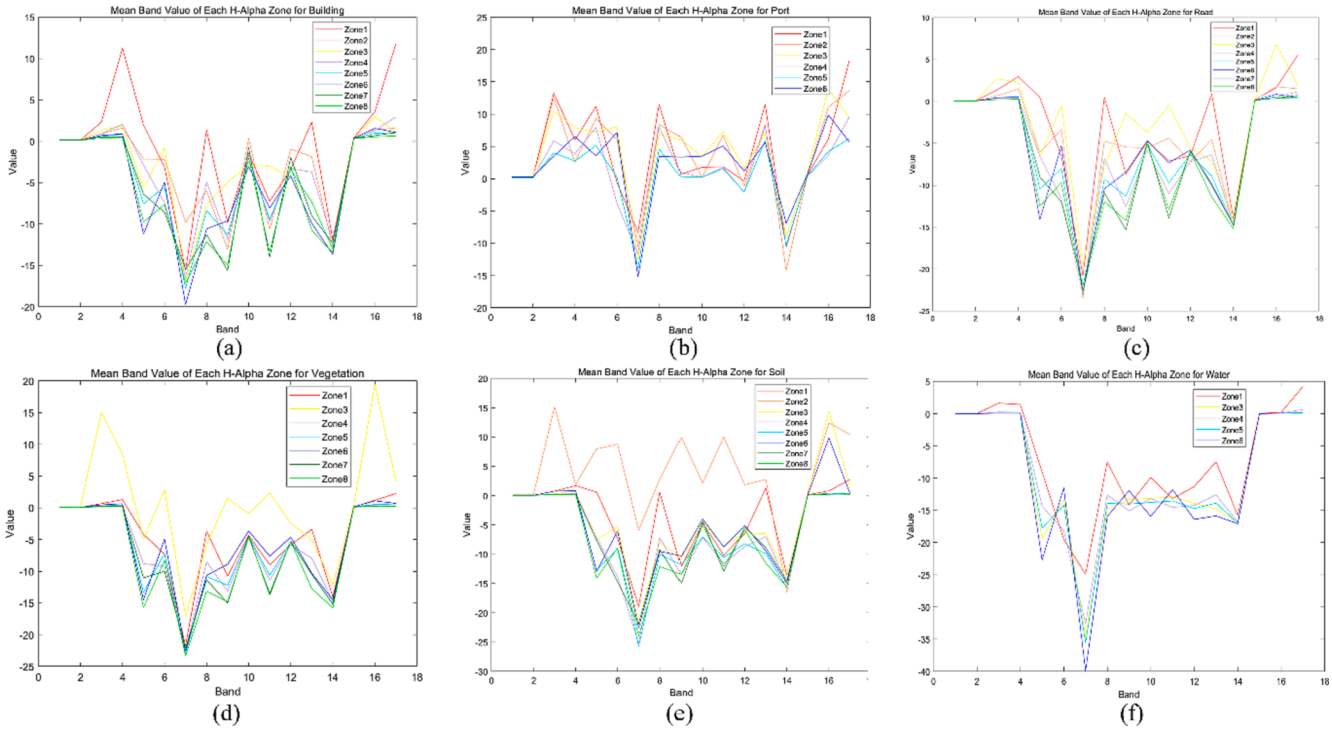

Fig. 8. The mean value of the polarimetric features on different H- α zones for each land cover. The abscissa axis represents the feature band, and the vertical axis represents the feature value.

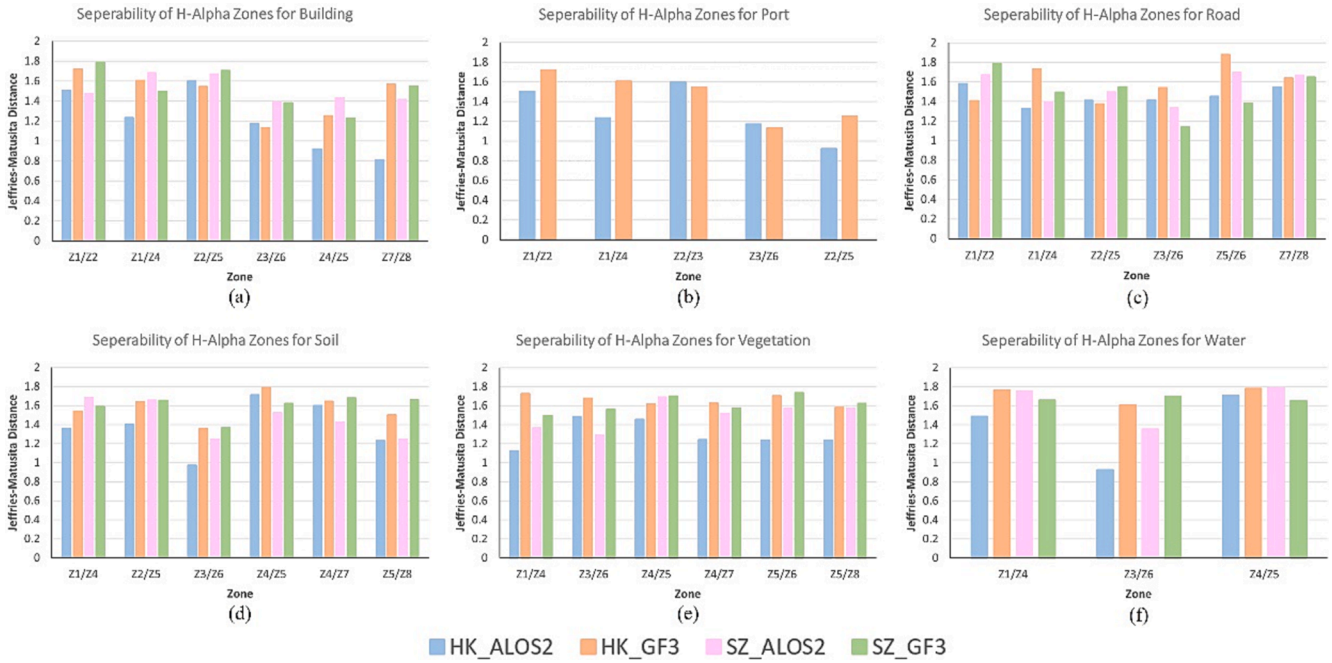

Fig. 9. Separability of H- α scattering zones for each land cover in HK and SZ with ALOS-2 and GF-3 data.

be mistaken for UIS or vegetation exhibiting volume scattering, as indicated in Fig. 10 (a-f). In optical images, water may be confused with dark UIS due to its low spectral reflectance, whereas in PolSAR, confusion between water and UIS primarily occurs between water and roads. Additionally, a lower level of confusion was observed in ALOS-2 compared to GF-3, potentially attributed to the lower spatial resolution and higher noise in GF-3. Finally, the land covers were merged into UIS and NIS, as demonstrated in Fig. 10 (m-r). The recognition results at this level exhibited high accuracy, as confusion within UIS (and NIS) sub-categories was effectively minimized.

To assess the effectiveness of the proposed PSMA-based classification system, a comparison was made with the fine-UIS oriented land cover classification scheme and the UIS&NIS classification scheme, as illustrated in Fig. 11. The proposed PSMA scheme in Fig. 11 represents the proposed land cover scattering sub-category classification scheme, while the traditional scheme (TS) corresponds to the fine-UIS land cover classification scheme and UIS&NIS classification scheme. The overall land cover classification accuracy achieved satisfactory levels and was

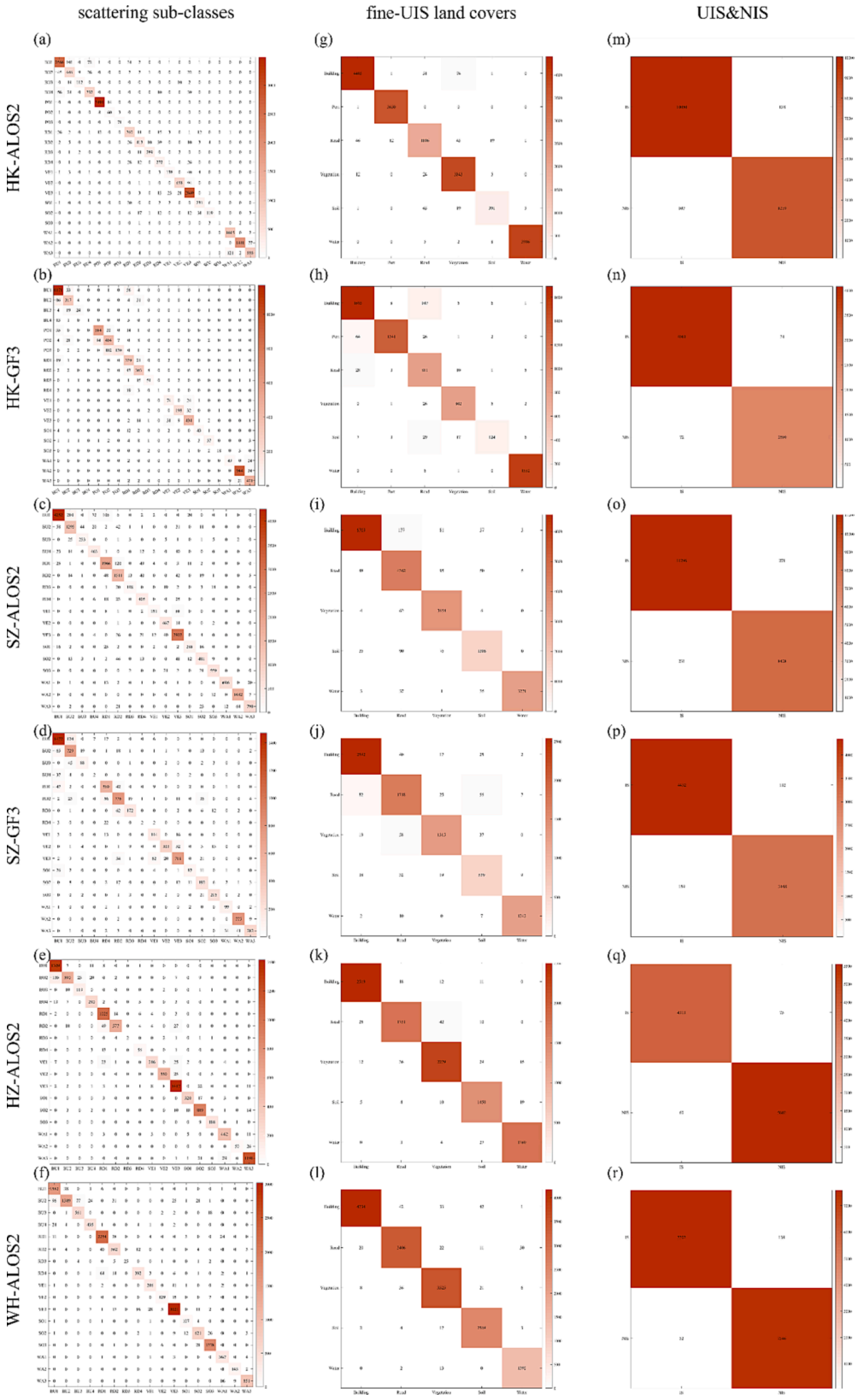

Fig. 10. Confusion matrix of the proposed scheme at the level of land cover scattering sub-categories (a-f), fine-UIS oriented land covers (g-l), and UIS&NIS (m-r) in HK, SZ, HZ, and WH with ALOS-2 and GF-3 images. The horizontal axis is the predicted category, and the vertical axis is the true category.

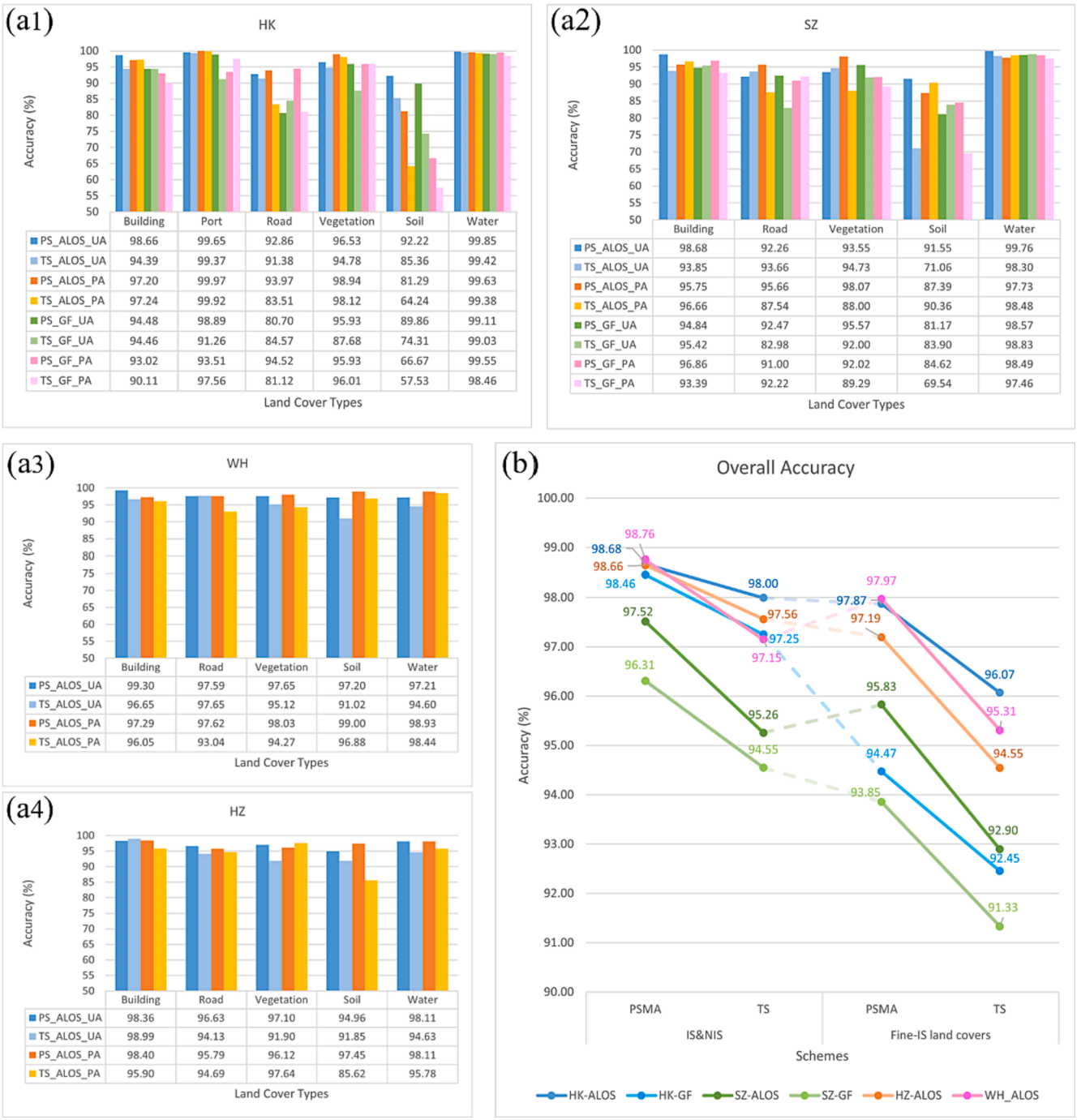

	Building	Port	Road	Vegetation	Soil	Water
PS_ALOS_UA	98.66	99.65	92.86	96.53	92.22	99.85
TS_ALOS_UA	94.39	99.37	91.38	94.78	85.36	99.42
PS_ALOS_PA	97.20	99.97	93.97	98.94	81.29	99.63
TS_ALOS_PA	97.24	99.92	83.51	98.12	64.24	99.38
PS_GF_UA	94.48	98.89	80.70	95.93	89.86	99.11
TS_GF_UA	94.46	91.26	84.57	87.68	74.31	99.03
PS_GF_PA	93.02	93.51	94.52	95.93	66.67	99.55
TS_GF_PA	90.11	97.56	81.12	96.01	57.53	98.46

	Building	Road	Vegetation	Soil	Water
PS_ALOS_UA	98.68	92.26	93.55	91.55	99.76
TS_ALOS_UA	93.85	93.66	94.73	71.06	98.30
PS_ALOS_PA	95.75	95.66	98.07	87.39	97.73
TS_ALOS_PA	96.66	87.54	88.00	90.36	98.48
PS_GF_UA	94.84	92.47	95.57	81.17	98.57
TS_GF_UA	95.42	82.98	92.00	83.90	98.83
PS_GF_PA	96.86	91.00	92.02	84.62	98.49
TS_GF_PA	93.39	92.22	89.29	69.54	97.46

	Building	Road	Vegetation	Soil	Water
PS_ALOS_UA	99.30	97.59	97.65	97.20	97.21
TS_ALOS_UA	96.65	97.65	95.12	91.02	94.60
PS_ALOS_PA	97.29	97.62	98.03	99.00	98.93
TS_ALOS_PA	96.05	93.04	94.27	96.88	98.44

	Building	Road	Vegetation	Soil	Water
PS_ALOS_UA	98.36	96.63	97.10	94.96	98.11
TS_ALOS_UA	98.99	94.13	91.90	91.85	94.63
PS_ALOS_PA	98.40	95.79	96.12	97.45	98.11
TS_ALOS_PA	95.90	94.69	97.64	85.62	95.78

Fig. 11. Producer's Accuracy (PA) and User's Accuracy (UA) of the proposed PSMA scheme and traditional scheme (TS) at the level of fine-UIS oriented land covers (a). (b) shows the overall accuracy at the level of fine-UIS oriented land covers and UIS&NIS level.

found to be comparable to the results reported in previous studies utilizing optical data (Li et al., 2020; Zhang et al., 2017).

In Fig. 11 (a), the proposed PSMA scheme exhibited significant improvement compared to the fine-UIS oriented land cover scheme. Consistent performance was observed across the four study areas. Notably, the proposed scheme yielded improvements in producer's accuracy (PA) for roads of approximately 4.6 % in WH, 8.1 % in SZ, and 13.4 % in HK. Additionally, the user's accuracy (UA) for roads saw an increase of up to 9.5 % with GF-3 in SZ, indicating a substantial reduction in road confusion compared to the traditional scheme. For buildings, improvements in UA reached up to 4.8 % with ALOS-2 and 3.5 % in PA with GF-3 in SZ. The port category also demonstrated higher accuracy with the proposed PSMA scheme, although there was a 4 % decrease in PA with GF-3 in HK, the UA increased by 7.6 %. Vegetation exhibited significant improvements of approximately 8.6 % in UA and 10 % in PA with GF-3 and ALOS-2 in HK and SZ. Soil showed substantial improvements of 20.5 % (15.5 %) in UA and 15.1 % (17 %) in PA in SZ (HK), while HZ and WH witnessed an increase of 11.8 % in PA and 6.2 % in UA for soil. Water achieved the highest accuracy among all land covers, with improvements of up to 3.5 % in HZ. Furthermore, in Fig. 11 (b), it is evident that the proposed PSMA scheme consistently outperformed the fine-UIS land cover scheme and the UIS&NIS scheme, with an overall accuracy (OA) improvement of up to 2.93 % and 2.26 %, respectively. These quantitative results demonstrate that the proposed

land cover scattering sub-category scheme effectively enhances land cover recognition by considering the scattering mechanisms within traditional land cover classes.

4.4. UIS mapping performance comparison

To provide a comprehensive assessment, Fig. 12 shows the land cover classification results for Hong Kong and Shenzhen using ALOS-2 and GF-3 (Fig. 12 (1)), and for Hangzhou and Wuhan using ALOS-2 (Fig. 12 (2)) at different levels of land cover types. Fig. 12 (a) presents the classification map at the level of land cover scattering sub-categories. It displays various shades of red for the sub-classes of buildings, with BU1, representing double bounce scattering, being the most prominent. Roads were primarily located in RO1 and RO2, characterized by double bounce scattering and volume scattering, respectively. Water was also divided into three sub-classes with different shades of blue. Among the vegetation sub-classes, VE3, characterized by volume scattering, was the most dominant. The subclasses were then combined to form land covers with the same definition as in optical images for further analysis, as in Fig. 12 (b). In general, it achieved relatively accurate recognition results on all cities and SAR data types, although there were still places for misrecognition. The recognition

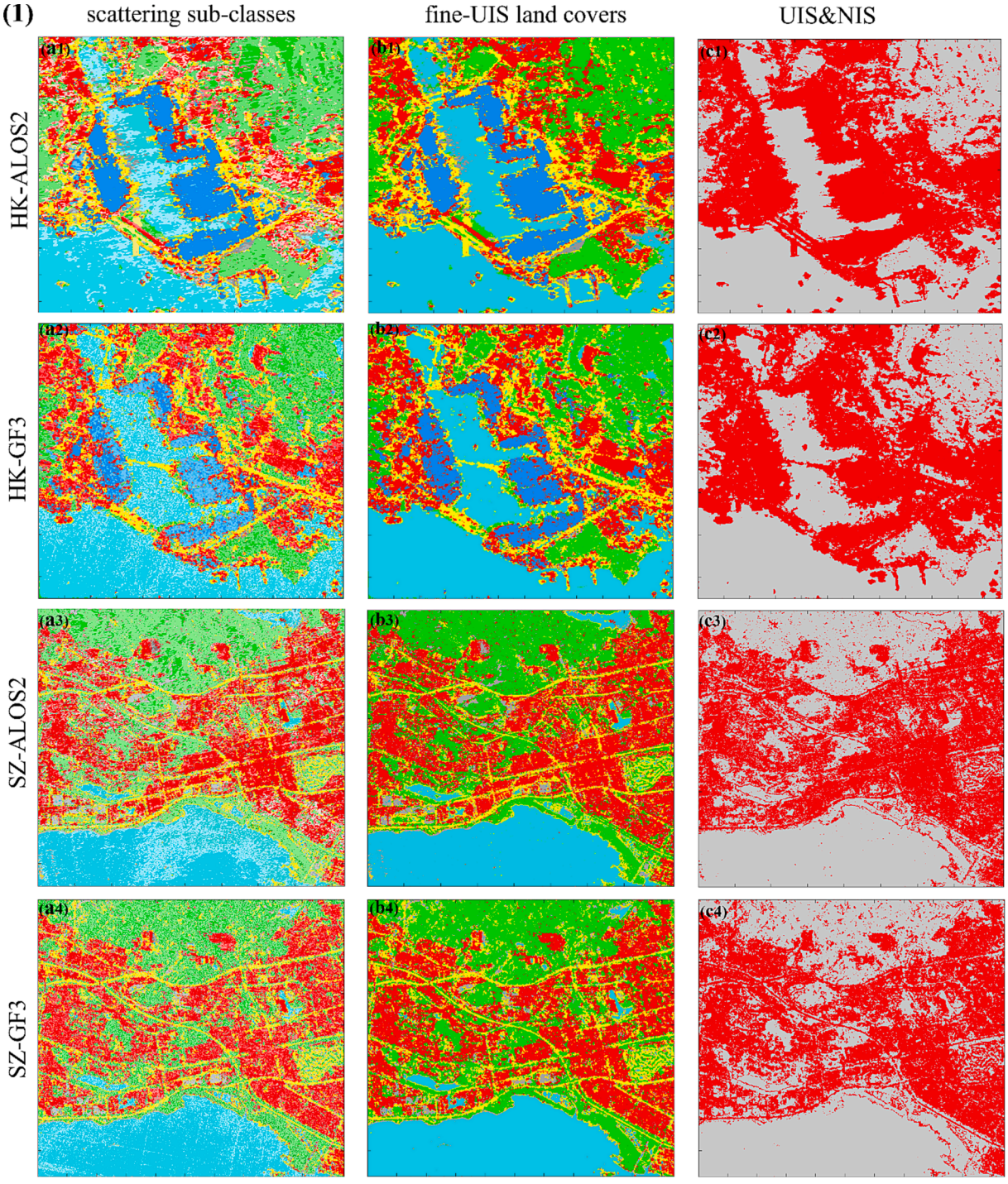

Fig. 12. Land cover classification results (1) for Hong Kong and Shenzhen with ALOS-2 and GF-3, and (2) for Hangzhou and Wuhan with ALOS-2 at the level of land cover scattering sub-categories (a), combined fine-UIS oriented land covers (b), and combined UIS and NIS (c).

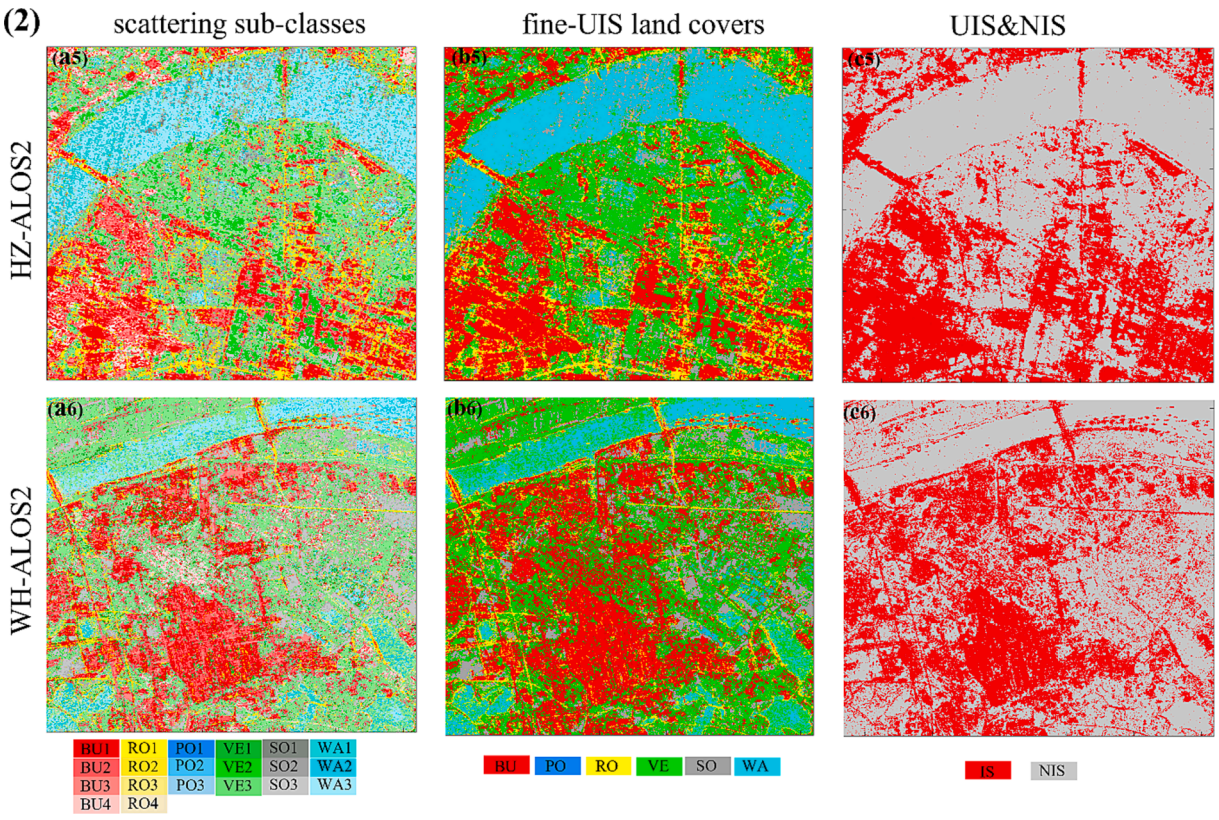

Fig. 12. (*continued*).

results for UIS subcategories were also relatively good, especially port, which was clearly recognized. Also, road was well-identified, displaying a clear shape and outline in both ALOS-2 and GF-3. Finally, the classified UIS and NIS in Fig. 12 (c) reflected a large proportion of impervious surfaces in all cities, indicating the high degree of urbanization of these cities.

To further evaluate the effectiveness of the new scheme, we compared its classification maps with those of the traditional schemes in more detail, at the level of land cover classification and impervious surface identification. The results are shown in Fig. 13.

Compared to the traditional scheme, the proposed scheme showed a reduction in confusion between UIS subclasses, such as the misclassification of roads as ports in Fig. 13 (a) and the misclassification of ports as buildings in Fig. 13 (c) and Fig. 13 (e). Regarding confusion between UIS and NIS, the proposed scheme also achieved better recognition for complex roads, such as the thin viaduct with a height difference from below roads, which was recognized as a continuous road shown in yellow in Fig. 13 (d), whereas the traditional scheme confused it as vegetation. The mitigation of underestimation of the road was also reflected by the considerable improvement of PA in Fig. 11. Additionally, the proposed scheme reduced confusion between water and soil in nearshore water bodies due to the interference of waves and facilities such as jacks, as shown in Fig. 13 (a) and (b). With respect to UIS identification, the proposed scheme demonstrated more accurate recognition of complex UIS, such as viaducts, roads with vehicles, and multi-lane roads compared to the traditional scheme, which tended to only identify the middle main road, as seen in Fig. 13 (f) and (h). The proposed scheme was also able to accurately identify continuous roads surrounded by dense and tall vegetation, even with an isolation belt in the middle, as shown in Fig. 13 (j). For NIS, such as soil, the proposed scheme better identified the boundary (Fig. 13 (i)) and reduced confusion of soil in construction as UIS (Fig. 13 (g)). Overall, the proposed scheme not only allowed for a more accurate distinction between UIS and NIS but also reduced confusion inside UIS and NIS subtypes, especially in complex urban settings.

5. Discussion

5.1. The necessity of urban land cover polarimetric scattering analysis

The phenomenon of spectral confusion in optical images is widely recognized. To address this challenge, various methods such as the SMA method, spectrum unmixing method, VIS model, and bright & dark UIS model have been adopted in optical remote sensing. These methods are designed based on the differences in land surface materials' spectral properties. However, in SAR data, land covers are identified based on their scattering properties, which may not necessarily align with the land surface material characteristics. The scattering behavior of land covers and their scattering mixtures in SAR has not been well explored. Therefore, this study conducted a comprehensive analysis of land cover scattering in PolSAR data in urban areas. We found that the land cover scattering behavior was very complex, and the previous understanding of the land cover scattering mechanism was inadequate. We discovered that objects belonging to the same land cover class could exhibit vastly different scattering properties, whereas those belonging to different classes may display similar scattering behavior. This highlights the need for polarimetric scattering mixture analysis. Drawing inspiration from strategies used in optical data, we proposed a novel UIS classification method based on comprehensive polarimetric scattering mixture analysis. Our quantitative and qualitative experiments demonstrated the effectiveness of this method, showing significant improvements in UIS recognition compared to the traditional method, particularly in the case of complex scattering land covers. We attribute these results to our method's ability to account for the different scattering properties of the same land cover and divide them into different sub-categories, which reduces intra-category differences and enables each subtype to focus on distinguishing its specific scattering characteristic without interference.

This study has practical implications for urban management, notably

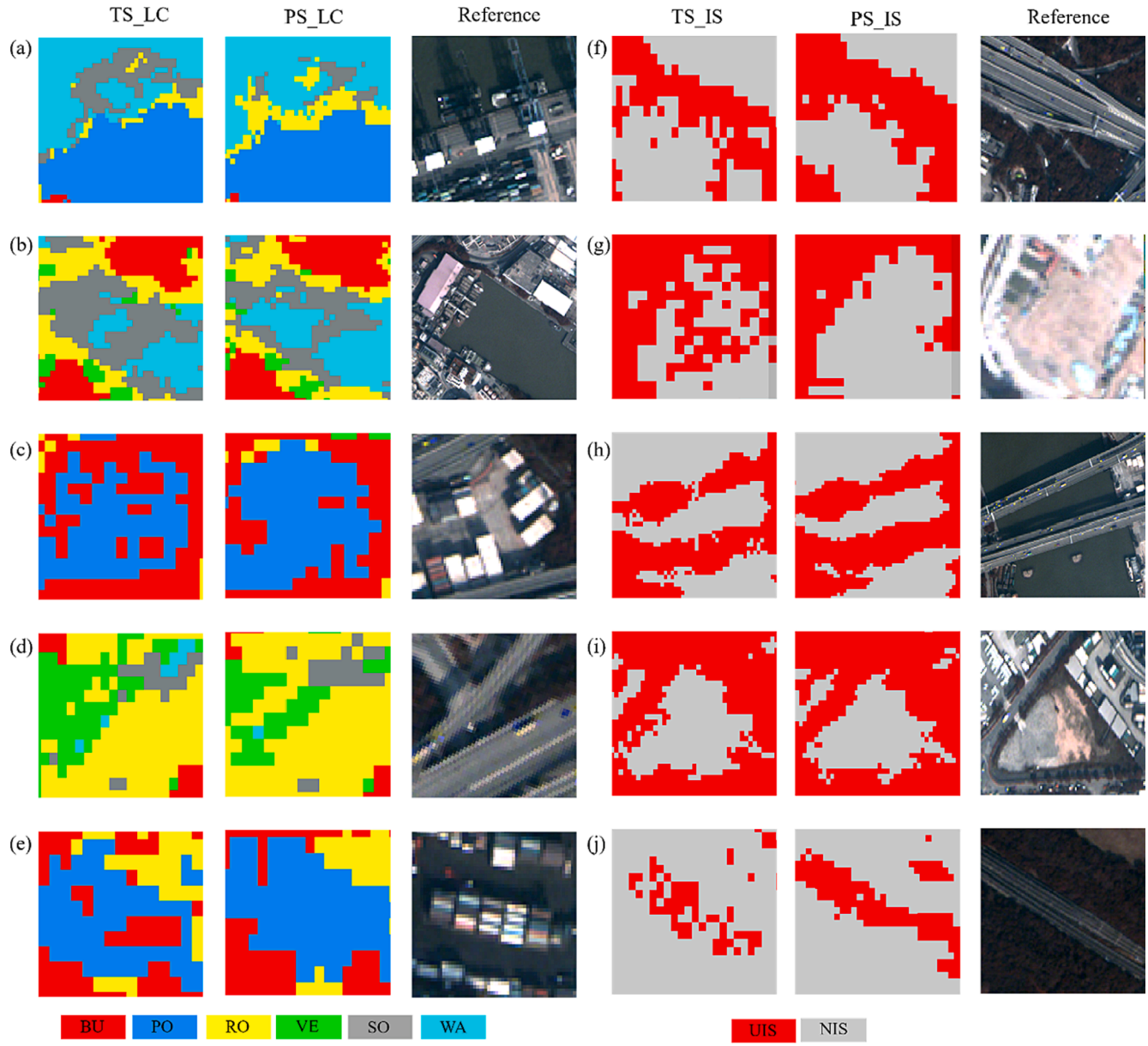

Fig. 13. Comparison of the land cover (columns 1–3) and UIS (columns 4–6) mapping results between the proposed scheme (PS) and traditional scheme (TS).

through improved fine-level urban land cover mapping accuracy and granularity. By utilizing SAR data and our PSMA method, urban areas can be accurately classified into finer categories, encompassing various building types, roads, vegetation, and water bodies. Such detailed information aids urban planners in making informed decisions regarding infrastructure development, resource allocation, and disaster management. Additionally, SAR data enables all-weather, cloud-independent, continuous surface observations, supporting real-time and uninterrupted urban surface status assessments.

5.2. Limitation of the proposed method

We utilized both ALOS-2 and GF-3 PolSAR data to ensure the universality of our proposed method for both C and L band fully PolSAR data. To avoid possible effects from land cover change, since these two data were not obtained at the same time, we carefully selected samples without land cover changes, with the help of high-resolution Worldview-2 and time-series Google Earth images. Although GF-3 and ALOS-2 differ in polarization frequency, band, spatial resolution, and angle of incidence, they both demonstrated consistent land cover scattering mixture phenomena and validated the effectiveness of our proposed method. One limitation of our study is that X-band fully polarimetric data was not applied due to difficulties in data acquisition. Further research with more polarization bands might help provide more information on urban land cover scattering mixture. Sample imbalance may affect the recognition of soil, as the number of soil samples is relatively smaller than that of other land covers, which is a real-world problem. Urbanization has led to an increase in impervious surfaces in cities, and while urban management seeks to preserve vegetation and water, bare soil is rare in cities, with most soil found under construction during the transition from NIS to UIS.

The integration of optical data holds significant potential to complement SAR data as optical data can provide valuable spectral and textural information that SAR data alone may lack. Currently, the fusion of optical and SAR data presents challenges, especially for our model, which is designed to address scattering confusions in SAR data specifically, making it unfeasible to directly apply our method to a straightforward fusion of optical and SAR data. However, the potential for the

fusion of optical and SAR data is substantial. The conceptual framework of our confusion analysis method is generalizable and can provide valuable insights for fusion. Further research will consider consolidating the land cover confusions from both optical and SAR data, with the goal of developing a comprehensive confusion model suitable for fused data.

5.3. Potential extensions to large-scale UIS mapping

To assess our model's applicability across various urban scenarios, we carefully selected four diverse regions in China, each representing different geographical and urban environments. While we recognize that urban scenarios can exhibit considerable variability beyond the specific regions we investigated, we posit that the fundamental principles governing the scattering responses of urban land cover elements remain consistent. Consequently, we anticipate that these principles will hold true across different urban environments. Just as our model demonstrated strong performance in the markedly distinct cities in our study, we believe it possesses the potential for broader applicability. Nevertheless, we acknowledge the need for careful consideration of specific details and nuances when adapting this model to larger-scale studies in various urban contexts. We will delve deeper into these issues in our forthcoming research endeavors.

The proposed method is not reliant on any specific classifier, terrain distribution, polarized band, or any other prior knowledge. It provides an effective and easily implementable UIS classification scheme based on the urban land cover scattering mixture. This approach demonstrates potential for large-scale UIS mapping, depending on the availability of C or L band fully PolSAR data. Considering the high cost of full-polarization SAR data, we acknowledge the practicality and accessibility of dual-polarization SAR data for large-scale applications, which offers advantages in terms of ease of acquisition and scalability. Despite differences between full-polarization and dual-polarization data, the underlying principles of scattering mixture analysis remain consistent, enabling the potential adaptation of our method to dual-polarization data. Our upcoming research will emphasize the analysis of urban land cover scattering mixtures using dual-polarization data to facilitate large-scale UIS mapping.

6. Conclusions

This study aimed to tackle the challenge of accurately identifying UIS by addressing the issue of land cover confusion in SAR data. A comprehensive analysis of urban land cover scattering mixtures was conducted, leading to the development of a novel UIS identification method based on urban land cover scattering modeling, which takes into account the scattering mechanisms. The evaluation of the method was carried out using C and L band PolSAR data in four Chinese cities, employing three levels of qualitative and quantitative experimental assessments to validate its effectiveness. The confusion analysis revealed the complex and diverse scattering behaviors within urban land covers, emphasizing the need to separate land cover scattering into specific scattering sub-categories for accurate classification. Experimental results highlighted the high overall accuracy achieved by the proposed PSMA method, reaching up to 98.76 % in HK. Compared to traditional methods, the proposed PSMA approach significantly reduced recognition confusion between UIS subclasses, UIS and NIS, and NIS subclasses. It achieved notable improvements for UIS, particularly for 'road', with enhancements of up to 13.4 %. Non-impervious surfaces such as soil and vegetation demonstrated significant accuracy improvements, with gains of up to 10 % and 20.5 % in PA and UA respectively. This study contributes to the understanding of land cover scattering mixtures and offers a promising approach for enhancing UIS identification accuracy in urban areas using PolSAR data.

Funding

This study was jointly supported by the International Research Center of Big Data for Sustainable Development Goals (CBAS2022GSP04), the Research Grants Council (RGC) of Hong Kong, China (HKU27602020, HKU17613022, HKU14605917), the National Natural Science Foundation of China (42022061 and 42071390), the Shenzhen Science and Technology Program (JCYJ20210324124013037) and the Seed Funding for Strategic Interdisciplinary Research Scheme of The University of Hong Kong.

CRediT authorship contribution statement

Jing Ling: Formal analysis, Methodology, Validation, Visualization, Writing – original draft. **Shan Wei:** Data curation, Writing – review & editing. **Paolo Gamba:** Writing – review & editing. **Rui Liu:** Data curation. **Hongsheng Zhang:** Conceptualization, Resources, Writing – review & editing, Funding acquisition.

Declaration of Competing Interest

The authors declare that they have no known competing financial interests or personal relationships that could have appeared to influence the work reported in this paper.

Data availability

Data will be made available on request.

References

Arnold Jr, C.L., Gibbons, C.J., 1996. Impervious surface coverage: the emergence of a key environmental indicator. J. Am. Plann. Assoc. 62, 243–258.
Attarchi, S., 2020. Extracting impervious surfaces from full polarimetric SAR images in different urban areas. Int. J. Remote Sens. 41, 4644–4663.
Cao, Y., Wu, Y., Zhang, P., Liang, W., Li, M., 2019. Pixel-Wise PolSAR Image Classification via a Novel Complex-Valued Deep Fully Convolutional Network. Remote Sens. 11, 2653.
Clinton, N., Yu, L., Gong, P., 2015. Geographic stacking: Decision fusion to increase global land cover map accuracy. ISPRS J. Photogramm. Remote Sens. 103, 57–65.
Cloude, S.R., Pottier, E., 1996. A review of target decomposition theorems in radar polarimetry. IEEE Trans. Geosci. Remote Sens. 34, 498–518.
Dabboor, M., Howell, S., Shokr, M., Yackel, J., 2014. The Jeffries-Matusita distance for the case of complex Wishart distribution as a separability criterion for fully polarimetric SAR data. Int. J. Remote Sens. 35, 6859–6873.
Devlin, J., Chang, M.-W., Lee, K., Toutanova, K., 2018. Bert: Pre-training of deep bidirectional transformers for language understanding. arXiv preprint arXiv: 1810.04805.
Dey, S., Mandal, D., Robertson, L.D., Banerjee, B., Kumar, V., McNairn, H., Bhattacharya, A., Rao, Y., 2020. In-season crop classification using elements of the Kennaugh matrix derived from polarimetric RADARSAT-2 SAR data. Int. J. Appl. Earth Obs. Geoinf. 88, 102059.
Freeman, A., Durden, S.L., 1998. A three-component scattering model for polarimetric SAR data. IEEE Trans. Geosci. Remote Sens. 36, 963–973.
Guo, H., Yang, H., Sun, Z., Li, X., Wang, C., 2014. Synergistic use of optical and PolSAR imagery for urban impervious surface estimation. Photogramm. Eng. Rem. Sens. 80, 91–102.
Homayouni, S., McNairn, H., Hosseini, M., Jiao, X., Powers, J., 2019. Quad and compact multitemporal C-band PolSAR observations for crop characterization and monitoring. Int. J. Appl. Earth Obs. Geoinf. 74, 78–87.
King, M.D., Platnick, S., Menzel, W.P., Ackerman, S.A., Hubanks, P.A., 2013. Spatial and temporal distribution of clouds observed by MODIS onboard the Terra and Aqua satellites. IEEE Trans. Geosci. Remote Sens. 51, 3826–3852.
Li, G., Li, L., Lu, D., Guo, W., Kuang, W., 2020. Mapping impervious surface distribution in China using multi-source remotely sensed data. GISci. Remote Sens. 57, 543–552.
Lin, Y., Wan, L., Zhang, H., Wei, S., Ma, P., Li, Y., Zhao, Z., 2021. Leveraging optical and SAR data with a UU-Net for large-scale road extraction. Int. J. Appl. Earth Obs. Geoinf. 103, 102498.
Ling, J., Zhang, H., Lin, Y., 2021. Improving Urban Land Cover Classification in Cloud-Prone Areas with Polarimetric SAR Images. Remote Sens. 13, 4708.
Ling, J., Zhang, H., 2023. WCDL: A Weighted Cloud Dictionary Learning Method for Fusing Cloud-Contaminated Optical and SAR Images. IEEE J. Sel. Top. Appl. Earth Obs. Remote Sens. 16, 2931–2941.
Liu, F., Jiao, L., Tang, X., 2019. Task-Oriented GAN for PolSAR Image Classification and Clustering. IEEE Trans Neural Netw. Learn Syst. 30, 2707–2719.

Liu, Z., Lin, Y., Cao, Y., Hu, H., Wei, Y., Zhang, Z., Lin, S., Guo, B., 2021. Swin transformer: Hierarchical vision transformer using shifted windows. Proc. IEEE Int. Conf. Comput. Vis. 10012–10022.
Mugiraneza, T., Hafner, S., Haas, J., Ban, Y., 2022. Monitoring urbanization and environmental impact in Kigali, Rwanda using Sentinel-2 MSI data and ecosystem service bundles. Int. J. Appl. Earth Obs. Geoinf. 109, 102775.
Pottier, E., Cloude, S.R., 1997. Application of the H/A/alpha polarimetric decomposition theorem for land classification, Wideband Interferometric Sensing and Imaging Polarimetry. SPIE 132–143.
Ridd, M.K., 1995. Exploring a VIS (vegetation-impervious surface-soil) model for urban ecosystem analysis through remote sensing: comparative anatomy for cities. Int. J. Remote Sens. 16, 2165–2185.
Samat, A., Gamba, P., Du, P., Luo, J., 2015. Active extreme learning machines for quad-polarimetric SAR imagery classification. Int. J. Appl. Earth Obs. Geoinf. 35, 305–319.
Samat, A., Gamba, P., Liu, S., Miao, Z., Li, E., Abuduwaili, J., 2018. Quad-PolSAR data classification using modified random forest algorithms to map halophytic plants in arid areas. Int. J. Appl. Earth Obs. Geoinf. 73, 503–521.
Shuster, W.D., Bonta, J., Thurston, H., Warnemuende, E., Smith, D., 2005. Impacts of impervious surface on watershed hydrology: A review. Urban Water J. 2, 263–275.
Tan, X., Li, M., Zhang, P., Wu, Y., Song, W., 2020. Complex-Valued 3-D Convolutional Neural Network for PolSAR Image Classification. IEEE Geosci. Remote Sens. Lett. 17, 1022–1026.
Tompkins, S., Mustard, J.F., Pieters, C.M., Forsyth, D.W., 1997. Optimization of endmembers for spectral mixture analysis. Remote Sens. Environ. 59, 472–489.
Vaswani, A., Shazeer, N., Parmar, N., Uszkoreit, J., Jones, L., Gomez, A.N., Kaiser, Ł., Polosukhin, I., 2017. Attention is all you need. Adv. Neural Inf. Process Syst 30.
Wu, C., Murray, A.T., 2003. Estimating impervious surface distribution by spectral mixture analysis. Remote Sens. Environ. 84, 493–505.
Yamaguchi, Y., Moriyama, T., Ishido, M., Yamada, H., 2005. Four-component scattering model for polarimetric SAR image decomposition. IEEE Trans. Geosci. Remote Sens. 43, 1699–1706.
Zhang, H., Lin, H., Wang, Y., 2018. A new scheme for urban impervious surface classification from SAR images. ISPRS J. Photogramm. Remote Sens. 139, 103–118.
Zhang, L., Weng, Q., Shao, Z., 2017. An evaluation of monthly impervious surface dynamics by fusing Landsat and MODIS time series in the Pearl River Delta, China, from 2000 to 2015. Remote Sens. Environ. 201, 99–114.